

A Quantum Framework for Negative Magnetoresistance in Multi-Weyl Semimetals

Arka Ghosh, Sushmita Saha and Alestin Mawrie

*Department of Physics, Indian Institute of Technology Indore, Simrol, Indore-452020, India**

(Dated: January 1, 2026)

We develop a fully quantum-mechanical theory of negative magnetoresistance in multi-Weyl semimetals in the $\mathbf{E} \parallel \mathbf{B}$ configuration, where the chiral anomaly is activated. The magnetotransport response is governed by Landau quantization and the emergence of multiple chiral Landau levels associated with higher-order Weyl nodes. These anomaly-active modes have unidirectional dispersion fixed by the node's monopole charge and dominate charge transport. As the magnetic field increases, individual chiral branches successively cross the Fermi energy, producing discrete slope changes in the longitudinal conductivity and a step-like negative magnetoresistance. This quantized evolution provides a direct experimental signature of multi-Weyl topology. Bulk Landau levels contribute only at very low fields due to strong disorder scattering and do not affect the anomaly-driven regime. Our results establish a unified, fully quantum-mechanical framework in which negative magnetoresistance arises from the discrete Landau-quantized spectrum and microscopic impurity scattering, beyond semiclassical anomaly descriptions.

I. INTRODUCTION

Negative magnetoresistivity (NMR) in the $\mathbf{E} \parallel \mathbf{B}$ geometry is a well-established transport signature of the chiral anomaly in Weyl and multi-Weyl semimetals. When electric and magnetic fields are aligned, the anomaly (the nonconservation of chiral charge induced by parallel \mathbf{E} and \mathbf{B}) pumps charge between Weyl nodes of opposite chirality, thereby enhancing the longitudinal conductivity and producing a characteristic decrease in resistivity^{1–5}. Despite its central role, most theoretical descriptions of NMR remain classical or semiclassical in nature, relying on Berry-curvature-modified Boltzmann equations, hydrodynamic anomaly relations, or semiclassical kinetic theory^{1,6}. Such approaches capture the anomaly-driven drift but do not resolve the microscopic Landau-level structure or the detailed influence of impurity scattering. A fully quantum framework is therefore required to understand how chiral Landau levels evolve with magnetic field, how their degeneracies are modified, and how their scattering rates shape the NMR response.

Weyl semimetals host a pair of band-touching points with linear or nonlinear dispersion^{7,8}. Each Weyl node acts as a quantized monopole of Berry curvature and carries a topological charge that governs anomalous transport and magneto-optical phenomena^{9,10}. Under a magnetic field this topological structure enforces the existence of a chiral Landau level with strictly unidirectional dispersion, which underlies the anomaly-induced enhancement of longitudinal conductivity in the $\mathbf{E} \parallel \mathbf{B}$ configuration^{11,12}.

Multi-Weyl semimetals (mWSMs) provide a natural generalization in which the nodes carry monopole charge $m > 1$, protected by crystalline rotational symmetries^{13,14}. Their transverse dispersion becomes nonlinear, and magnetic quantization yields m chiral Landau levels^{13,15}. The presence of multiple anomaly-active channels strengthens and reshapes the longitudinal transport response, thereby should give rise to enhanced, and in many cases multi-step-NMR profiles.

Candidate platforms include SrSi_2 , EuIn_2As_2 , strained MoTe_2 and WTe_2 , the LaAlGe family, kagome magnets such as $\text{Co}_3\text{Sn}_2\text{S}_2$, and chiral crystals such as AlPt and AlPd ^{16–30}. In these materials, the spacing between successive chiral Landau levels, $\Delta E_{\text{ch}} = E_{n+1}^{\text{ch}} - E_n^{\text{ch}}$, is set by magnetic-field-controlled Landau quantization and remains comparable to or larger than the thermal broadening $k_B T$ over the experimentally relevant field range $0.5 < B < 4.5$ T, as established for realistic Weyl and tilted Weyl systems in Refs. [31,32]. Thus, even at room temperature the chiral levels are well resolved, and transport along $\mathbf{E} \parallel \mathbf{B}$ proceeds through discrete quantum channels rather than semiclassical or hydrodynamic drift. This hierarchy provides strong motivation for a unified, fully quantum description of NMR across different topological charges.

While semiclassical formulations such as those of Son & Spivak¹ and Spivak & Andreev⁶ successfully predict a linear-in- B magnetoconductivity, they treat the anomaly-induced current as a continuum drift process and therefore cannot capture the microscopic structure that emerges under Landau quantization. In particular, semiclassical theories do not resolve (i) the discrete set of m chiral Landau levels fixed by the monopole charge, (ii) the field-dependent depopulation of individual chiral branches, or (iii) the resulting sequence of kinks and piecewise-linear segments in $\sigma_{zz}(B)$. The present work goes beyond these approaches by developing a fully quantum, Landau-level-resolved theory of magnetotransport in which the m chiral modes govern the anomaly-induced conductivity. A central result is the identification of characteristic magnetic fields B_n at which the n^{th} chiral Landau level crosses the Fermi energy and ceases to contribute to transport. This mechanism produces the multi-step structure of $\sigma_{zz}(B)$ and the corresponding kinks in the magnetoresistance-direct fingerprints of the node's topological charge with no analogue in semiclassical theories. Although both semiclassical and quantum approaches predict an overall negative magnetoresistance, the microscopic origin, internal structure, and

field-dependent signatures identified here are uniquely quantum and arise directly from the Landau-quantized spectrum of multi-Weyl fermions.

In this work, we develop such a fully quantum-mechanical framework for NMR in Weyl and multi-Weyl semimetals. Our theory incorporates the complete Landau-level spectrum, screened Coulomb disorder, and the Kubo formalism, enabling a transparent treatment of both chiral and bulk channels. We show that the anomaly-induced NMR profile is dictated by the number of chiral branches: triple-Weyl semimetals ($m = 3$) exhibit three distinct linear regimes in $\sigma_{zz}(B)$, double-Weyl systems ($m = 2$) display two, and ordinary Weyl nodes ($m = 1$) show a single smooth linear increase without intermediate structure. Whenever a chiral branch is pushed above the Fermi level, its contribution vanishes abruptly, producing an observable change in slope. These features emerge naturally within our quantum treatment and cannot be reproduced using semiclassical anomaly theories.

The remainder of this paper presents the full derivations, demonstrating how topology, Landau quantization, and microscopic impurity scattering combine to produce the chiral-anomaly-induced NMR response in Weyl and multi-Weyl semimetals.

II. HAMILTONIAN FORMULATION AND EMERGENCE OF CHIRAL STATES

The low-energy excitations of Weyl and multi-Weyl semimetals are governed by topologically protected band-touching points whose monopole charge determines the degree of anisotropy and non-linearity in their dispersion. For a multi-Weyl node of order m , the minimal continuum Hamiltonian can be written as

$$H_0 = \frac{\lambda}{2} \left(k_-^m \sigma_+ + k_+^m \sigma_- \right) + \eta v_z \left(k_z + \eta \frac{Q}{2} \right) \sigma_z, \quad (1)$$

where $\sigma_{x,y,z}$ are the Pauli matrices acting on the pseudospin basis, $\sigma_{\pm} = \sigma_x \pm i\sigma_y$, and $k_{\pm} = k_x \pm ik_y$. The parameter λ determines the strength of the in-plane non-linearity, v_z is the band velocity along k_z , and Q is the momentum-space separation between the two Weyl nodes of chirality $\eta = \pm 1$. The integer m plays the role of the monopole charge of the Berry curvature and determines both the topological and spectroscopic properties of the node.¹³ Also, this Hamiltonian correctly reproduces the anisotropic dispersion observed in density-functional calculations and tight-binding models of multi-Weyl systems^{13,33}.

Inclusion of a tilt and quadratic particle-hole asymmetry term: In many Weyl and multi-Weyl materials, the dispersion around the node is not perfectly upright but acquires a finite tilt along a crystallographic direction. This tilt preserves the Weyl point but reshapes the energy cone and, when sufficiently strong, drives a

Type-I to Type-II transition marked by touching electron and hole pockets.^{31,32} Given its pronounced impact on the density of states and transport coefficients, the tilt must be included for a realistic description. In addition to the linear Weyl dispersion, realistic band structures generally exhibit particle-hole asymmetry arising from higher-order momentum terms. This effect is modeled by including a quadratic contribution in the transverse plane, which preserves the Weyl point and does not affect its topology, but modifies the Landau-level spacing and transport response. Such particle-hole asymmetric corrections are commonly retained in low-energy descriptions of tilted and non-ideal Weyl systems.^{31,32} Below we incorporate the above correction terms into the Hamiltonian and study how it modifies both the chiral Landau levels and the global Landau-level structure.

$$H_{\text{tilt}} = w_{\parallel} (k_x^2 + k_y^2) \sigma_0 + w_z k_z \sigma_0, \quad (2)$$

which does not gap out the Weyl point but shifts and skews the cones. Here H_{tilt} , collectively denotes the scalar terms responsible for the longitudinal tilt of the Weyl cones and the particle-hole asymmetry of the spectrum. We tabulate the system parameters as follows [I]

Monopole charge	v_z	w_z	λ	w_{\parallel}
$m = 1$	1.0	0.25 v_z	0.30	0.20
$m = 2$	1.5	0.25 v_z	0.30	0.8 λ
$m = 3$	2.0	0.25 v_z	0.60	0.30

TABLE I: Model parameters used in this work. The chosen values lie within experimentally measured and first-principles-calculated ranges for Weyl and multi-Weyl semimetals. For $m = 1$, typical band velocities and tilt strengths are guided by ARPES and *ab initio* studies of TaAs and NbP (see Refs.[25–27]). For $m = 2$, the nonlinear dispersion parameter λ and the anisotropy v_z/λ are taken to be consistent with double-Weyl candidates such as SrSi₂ from first-principles calculations²⁸. For $m = 3$, the enhanced anisotropy and nonlinear coefficients reflect the cubic Weyl dispersion observed in multifold chiral crystals such as CoSi and RhSi, whose velocities and node separations have been established by ARPES and DFT (Refs.[29,30]). These references show that the adopted dimensionless ratios w_z/v_z , λ , and w_{\parallel} fall within realistic material-specific ranges, making the present model quantitatively representative of experimentally relevant multi-Weyl systems.

Landau quantization: To expose the chiral structure of the spectrum, we apply a magnetic field $\mathbf{B} = B\hat{z}$ and adopt the Landau gauge $\mathbf{A} = (-By, 0, 0)$. The canonical momenta transform as

$$\Pi_x = p_x - By, \quad \Pi_y = p_y, \quad (3)$$

and it is convenient to introduce the standard ladder operators

$$a = \frac{\Pi_x - i\Pi_y}{\sqrt{2B}}, \quad a^\dagger = \frac{\Pi_x + i\Pi_y}{\sqrt{2B}}, \quad (4)$$

which satisfy $[a, a^\dagger] = 1$. In terms of these operators, the total Hamiltonian in Eq. (1) becomes^{32,33}

$$H_T = 2Bw_{\parallel} \left(a^\dagger a + \frac{1}{2} \right) \sigma_0 + \begin{bmatrix} (w_z + \eta v_z)(k_z + \eta \frac{Q}{2}) & \lambda_m a^m \\ \lambda_m (a^\dagger)^m & (w_z - \eta v_z)(k_z + \eta \frac{Q}{2}) \end{bmatrix} \quad (5)$$

with $\lambda_m = \lambda(2B)^{m/2}$. This form highlights the fundamental distinction between single ($m = 1$) and multi-Weyl ($m > 1$) nodes: the magnetic field couples Landau oscillator states $|n\rangle$ to $|n - m\rangle$, rather than to $|n - 1\rangle$, reflecting the m -fold vortex structure in the transverse dispersion. For $n \geq m$, we thus have the trial spinor

$$\psi_{n,k_z}^{\eta,s} = \begin{pmatrix} \alpha_n^{\eta,s}(k_z) |n - m\rangle \\ \beta_n^{\eta,s}(k_z) |n\rangle \end{pmatrix}, \quad (6)$$

which yields the bulk Landau-level energies

$$E_n^{\eta,s}(k_z) = (2n - m + 1)Bw_{\parallel} + \hbar w_z \left(k_z + \eta \frac{Q}{2} \right) + s \Gamma_n^m, \quad (7)$$

with

$$\Gamma_n^m = \sqrt{\left[-mBw_{\parallel} + \eta v_z \left(k_z + \eta \frac{Q}{2} \right) \right]^2 + \frac{n!}{(n - m)!} \lambda_m^2}.$$

Also,

$$\begin{aligned} \alpha_n^{\eta,s}(k_z) &= \frac{1}{\sqrt{2}} \sqrt{1 - s \frac{Bmw_{\parallel} - \eta v_z(k_z + \eta \frac{Q}{2})}{\Gamma_n^m}} \\ \beta_n^{\eta,s}(k_z) &= \frac{1}{\sqrt{2}} \sqrt{1 + s \frac{Bmw_{\parallel} - \eta v_z(k_z + \eta \frac{Q}{2})}{\Gamma_n^m}} \end{aligned} \quad (8)$$

These modes are gapped away from the chiral Landau states and possess wavefunctions containing higher-order Hermite polynomials, whose increased oscillatory structure enhances their overlap with short-range disorder, making them more susceptible to impurity scattering.

Emergence of chiral states: For $n < m$, one cannot form the state $|n - m\rangle$, and the upper spinor component in Eq. (6) vanishes identically. The eigenvalue equation reduces to a single-component problem, producing

$$E_n^{\eta,\text{ch}}(k_z) = (w_z - \eta v_z) \left(k_z + \eta \frac{Q}{2} \right) + (2n + 1)Bw_{\parallel}. \quad (9)$$

with eigen-spinor equal to $(0, |n\rangle)^T$. These m modes constitute the celebrated chiral Landau levels, whose propagation direction is locked to the chirality η of the Weyl

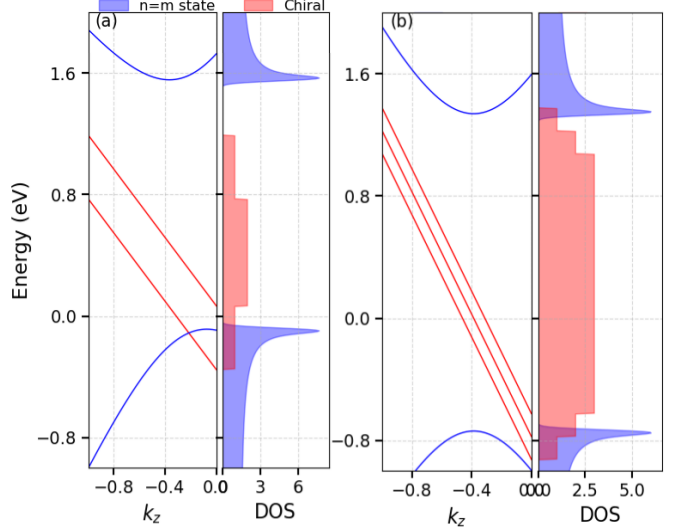


FIG. 1: Energy dispersion and density of states (DOS) of Landau-quantized multi-Weyl semimetals in a magnetic field. Panel (a) shows a double-Weyl node ($m = 2$) and panel (b) a triple-Weyl node ($m = 3$). In each case, the left plot displays the Landau-level spectrum versus k_z , while the right plot shows the corresponding DOS. Red lines denote the m chiral Landau levels with unidirectional dispersion fixed by the node chirality, and blue curves represent bulk ($n = m$) Landau levels.

node^{34,35}. This unique combination of features underlies the Adler-Bell-Jackiw chiral anomaly^{3,4,11} and is responsible for the characteristic linear in B enhancement of longitudinal conductivity in the longitudinal ($\mathbf{E} \parallel \mathbf{B}$) configuration. These chiral modes remain unidirectional, robust, and topologically protected as long as the tilt does not exceed the critical threshold separating type-I and type-II Weyl phases^{31,32}. Their presence and evolution with magnetic field are central to the quantum description of longitudinal magnetotransport and the emergence of NMR analyzed in later sections.

Density of States of Chiral States: Mathematically, the DOS of chiral states for Weyl semimetal with topological charge m can be written as,

$$\begin{aligned} \mathcal{D}_{\text{ch}}^{\eta}(E) &= \frac{1}{2\pi l_B^2} \sum_{n=0}^{m-1} \int \frac{dk_z}{2\pi} \delta(E - E_n^{\eta,\text{ch}}(k_z)) \\ &\times \Theta(E - E_n^{\eta,\text{min}}) \Theta(E_n^{\eta,\text{max}} - E), \end{aligned} \quad (10)$$

where the magnetic length $l_B = 1/\sqrt{B}$. Also, we defined $E_n^{\eta,\text{min}} = E_n^{\eta,\text{ch}}(k_z = 0)$ and $E_n^{\eta,\text{max}} = E_n^{\eta,\text{ch}}(k_z = Q)$ to be the maximum and minimum energy value of an n^{th}

chiral state, respectively, defined as

$$\left. \begin{aligned} E_n^{\eta,\min} &= (2n+1)w_{\parallel}B - (v_z - \eta w_z) \frac{\mathcal{Q}}{2}, \\ E_n^{\eta,\max} &= (2n+1)w_{\parallel}B + \mathcal{Q} \left(1 + \frac{\eta}{2}\right) (w_z - \eta v_z) \end{aligned} \right\}, \quad (11)$$

which specify the lowest and highest possible energy along the n^{th} chiral channel. These bounds arise because the chiral Landau level disperses linearly in k_z with slope determined by the combination $(w_z - \eta v_z)$, and terminates at the locations of the two Weyl nodes separated by momentum \mathcal{Q} . We derived the above quantities by adopting a fully linear dispersion (Eq. [9]) over the interval $0 < k_z < \mathcal{Q}$ because the experimentally relevant transport window lies entirely within the linear regime of the Weyl cone, well before lattice-scale curvature becomes appreciable near the two Weyl nodes at $k_z = 0$ and $k_z = \mathcal{Q}$.

After integration over the k_z space, we get the DOS of chiral state to be,

$$\begin{aligned} \mathcal{D}_{\text{ch}}^{\eta}(E) &= \frac{1}{4\pi^2 \ell_B^2 |w_z - \eta v_z|} \\ &\times \sum_{n=0}^{m-1} \Theta(E - E_n^{\eta,\min}) \Theta(E_n^{\eta,\max} - E). \end{aligned} \quad (12)$$

This result (in Fig. [1]) shows that the DOS of the chiral states is constant within each allowed energy window and inversely proportional to the chiral velocity $|w_z - \eta v_z|$. The existence of m distinct windows directly reflects the topological charge of the multi-Weyl node: higher monopole charge produces multiple chiral branches, each contributing a finite DOS. The presence of a nonzero chiral DOS, even at energies where the bulk DOS vanishes, is a key signature of Weyl physics in a magnetic field and plays an essential role in magnetotransport and magneto-optical phenomena such as the chiral anomaly and field-induced absorption features.

III. NEGATIVE MAGNETORESISTANCE

The interplay between Landau quantization and impurity scattering plays a central role in determining the transport properties of Weyl and multi-Weyl semimetals. In particular, when a magnetic field is applied parallel to the current direction, the emergence of chiral Landau levels leads to unconventional charge transport and a characteristic NMR. Understanding this behavior requires a detailed evaluation of the longitudinal conductivity, in which both the structure of the Landau-level wavefunctions and the corresponding scattering mechanisms computed earlier through the transport relaxation time τ^{tr} (See Appendix[A]) enter on equal footing. In this section, we combine the Kubo formalism to obtain analytical expressions for the conductivity originating from both chiral and bulk Landau levels, and we analyze how their

distinct wavefunction profiles control the overall magnetotransport response.

Longitudinal Conductivity: To understand charge transport in a magnetic field, we compute the longitudinal conductivity σ_{zz} using linear-response theory. In a Landau-quantized system, the current response to an applied electric field is determined not only by the band dispersion but also by the wavefunction structure of the Landau levels. The Kubo formula provides a convenient and fully quantum-mechanical framework to incorporate these effects, including disorder through the Green's functions.

We begin with the standard Kubo expression for dc conductivity³⁶⁻³⁸:

$$\sigma_{zz} = \frac{2\pi e^2 \hbar}{V} \int_{-\infty}^{\infty} dE \left[-\frac{\partial f(E)}{\partial E} \right] \text{Tr}[v_z G^R(E) v_z G^A(E)], \quad (13)$$

where $G^{R/A}$ denote the retarded and advanced Green's functions, $f(E)$ is the Fermi-Dirac distribution, and the velocity operator along the field direction is $v_z = \partial H / \partial k_z$.

In the Landau-level (LL) basis $|n, k_z, s\rangle$, the Green function takes the diagonal form

$$G^{R/A}(E) = \sum_{n, k_z, s} \frac{|n, k_z, s\rangle \langle n, k_z, s|}{E - E_n^s(k_z) \pm i\Gamma_n^s(k_z)}, \quad (14)$$

where $\Gamma_n^s(k_z) = 1/[2\tau_n^s(k_z)]$ represents the LL broadening and τ_n is the total scattering time associated with level n . Using this representation, the trace in Eq. (13) becomes

$$\text{Tr}[v_z G^R v_z G^A] = \sum_{n, k_y, k_z, s} |v_{z;n,s}(k_z)|^2 G_{n,s}^R(E; k_z) G_{n,s}^A(E; k_z), \quad (15)$$

where $|v_{z;n,s}(k_z)|^2 = |\langle n, k_z, s | v_z | n, k_z, s \rangle|^2$. The product of Green functions evaluates to

$$G_{n,s}^R(E; k_z) G_{n,s}^A(E; k_z) = \frac{1}{(E - E_n^s)^2 + (\Gamma_n^s)^2}. \quad (16)$$

We assume the width, Γ_n is small compared to the inter-LL spacing, the energy integral in Eq. (13) may be performed using the Lorentzian identity

$$\int_{-\infty}^{\infty} dE \frac{-\partial f / \partial E}{(E - \varepsilon)^2 + \Gamma^2} \simeq \frac{\pi}{\Gamma} \left[-\frac{\partial f}{\partial E} \right]_{E=\varepsilon} = 2\pi\tau_n^s \left[-\frac{\partial f}{\partial E} \right]_{E=E_n^s(k_z)}, \quad (17)$$

thereby producing a factor proportional to the LL lifetime τ_n^s . After performing the trace over the LL guiding-center quantum number k_y , which carries the degeneracy $L_x L_y / (2\pi \ell_B^2)$, and converting the remaining sum over k_z to an integral, we obtain

$$\sigma_{zz} = \frac{e^2 \hbar}{2\pi^2 \ell_B^2} \sum_{n,s} \int dk_z |v_{z;n,s}(k_z)|^2 \tau_{n,s}^{\text{tr}}(k_z) \left[-\frac{\partial f(E)}{\partial E} \right]_{E=E_n^s(k_z)}. \quad (18)$$

It is important to distinguish between the quantum (single-particle) lifetime τ^q and the transport lifetime

τ^{tr} . The quantum lifetime, defined through the imaginary part of the retarded self-energy, controls the spectral broadening of Landau levels and determines the width of single-particle excitations. In contrast, the transport lifetime accounts for momentum relaxation and incorporates the angular weighting $(1 - \cos \theta)$ that suppresses forward scattering events. As a result, τ^{tr} governs the decay of electrical current and is the relevant timescale entering the Kubo formula for the longitudinal conductivity σ_{zz} . Throughout this work we therefore replace the total lifetime by τ^{tr} , which is evaluated microscopically from screened Coulomb disorder in Appendix A.

A. Contribution from impurity-induced self-scattering of chiral states:

As stated earlier, the chiral Landau levels, present for $0 \leq n \leq m - 1$, exhibit strictly linear dispersion in k_z (Eq. [9]) and are topologically protected^{11,39}. Using the chiral transport relaxation time derived in Eq. [A19], the above Eq. (18) becomes

$$\begin{aligned} & \text{Tr} \left[v_z G_n^{\eta R}(E) v_z G_{n'}^{\eta A}(E) \right] \\ &= 2\pi |w_z - \eta v_z|^2 \sum_{n=0}^{m-1} \mathcal{D}_{\text{ch}}^{\eta}(E) \frac{\tau_0}{\mathcal{I}_n^{\eta, \text{ch}}}. \end{aligned} \quad (19)$$

where $\mathcal{D}_{\text{ch}}^{\eta}(E)$ is the DOS for the chiral states and $\mathcal{I}_n^{\eta, \text{ch}}$ is the dimensionless angular integral calculated in the Eq. [A20] of the Appendix with τ_0 also defined in the same appendix. At $T = 0$ K, the derivative of the Fermi distribution becomes a delta function, and Eq. [13] thus yields

$$\sigma_{zz}^{\eta} = \sigma_0 B \sum_{n=0}^{m-1} \frac{\Theta(E_F - E_n^{\eta, \text{min}}) \Theta(E_n^{\eta, \text{max}} - E_F)}{\mathcal{I}_n^{\eta, \text{ch}}}, \quad (20)$$

with $\sigma_0 = e^2 |v_z| \tau_0 / l_B^2$. The steps associated with multiple chiral channels become broadened, but the linear-in- B trend persists.

B. Bulk self-scattering and the dominance of the $n = m$ Landau level

Using the Eq. (A25) and the velocity matrix element for the bulk state $|v_{z; n, s}^{\eta}(k_z)|^2 = [(w_z + \eta v_z)|\alpha_n^{\eta, s}(k_z)|^2 + (w_z - \eta v_z)|\beta_n^{\eta, s}(k_z)|^2]^2$, the longitudinal conductivity can be evaluated from Eq. (18). This incorporates the full k_z dependence of the velocity matrix element, wavefunction amplitudes, and impurity-induced scattering rate. Although bulk levels with $n > m$ formally appear in the Kubo sum, they may be safely omitted when computing $\sigma_{zz}(B)$ for the parameter regime of interest. The primary reason is energetic: for the chosen Fermi level ($E_F = 200$ meV),

all bulk Landau levels with $n > m$ lie far above or below the Fermi level for any field in the regime ($B \gtrsim 0.3\text{--}0.5$ T) and therefore remain unoccupied throughout the range where negative magnetoresistance is observed. Their exclusion thus does not remove any physically accessible transport channel.

The following auxiliary considerations further support this simplification. (i) Higher bulk Landau levels possess increasingly oscillatory transverse wavefunctions, which strongly enhance their overlap with disorder and produce rapidly growing scattering rates and correspondingly short transport lifetimes. (ii) Even the lowest bulk level contributes only a small, short-lived background at very low fields, while including levels with $n > m$ alters $\sigma_{zz}(B)$ by less than 10^{-4} yet substantially increases numerical cost. (iii) All experimentally relevant features, the growth of the m chiral channels, the multi-segment structure of $\sigma_{zz}(B)$ for $m > 1$, and the resulting negative magnetoresistance are governed exclusively by the m chiral Landau levels ($n < m$) together with the lowest bulk level ($n = m$). Higher bulk levels introduce no new qualitative behavior and make no observable quantitative contribution.

For these reasons, retaining only the $n = m$ bulk Landau level captures all physically relevant contributions from the bulk states while remaining fully consistent with the quantum mechanics of multi-Weyl fermions.

C. Negative Magnetoresistance

The magnetoresistance (MR) in the $\mathbf{E} \parallel \mathbf{B}$ configuration is defined as

$$\text{MR}(B) = \frac{\rho_{zz}(B) - \rho_{zz}(0)}{\rho_{zz}(0)} = \frac{\sigma_{zz}(0)}{\sigma_{zz}(B)} - 1, \quad (21)$$

where $\rho_{zz} = 1/\sigma_{zz}$ and the longitudinal conductivity $\sigma_{zz}(B)$ is obtained by combining the chiral and bulk contributions. A negative value of MR signals an enhancement of σ_{zz} with increasing field—an effect that arises microscopically from the chiral anomaly and the field-enhanced degeneracy of the chiral Landau levels. Figure 2 summarizes the full magnetotransport response of multi-Weyl semimetals. For the double-Weyl case ($m = 2$), Fig. 2(a) shows that the two chiral Landau levels generate two distinct linear regimes in $\sigma_{zz}(B)$, each associated with one chiral branch remaining at the Fermi level. The bulk background in Fig. 2(b), contributes only at small B because higher-order Landau level wavefunctions couple strongly to disorder and thus exhibit short transport lifetimes. Consequently, the total conductivity is dominated by the chiral states over most of the field range, producing a two-stage rise that directly translates into the negative MR curve of Fig. 2(d). This behavior reflects the progressive activation of chiral channels as the magnetic field grows, a feature absent in semiclassical descriptions^{1,4}.

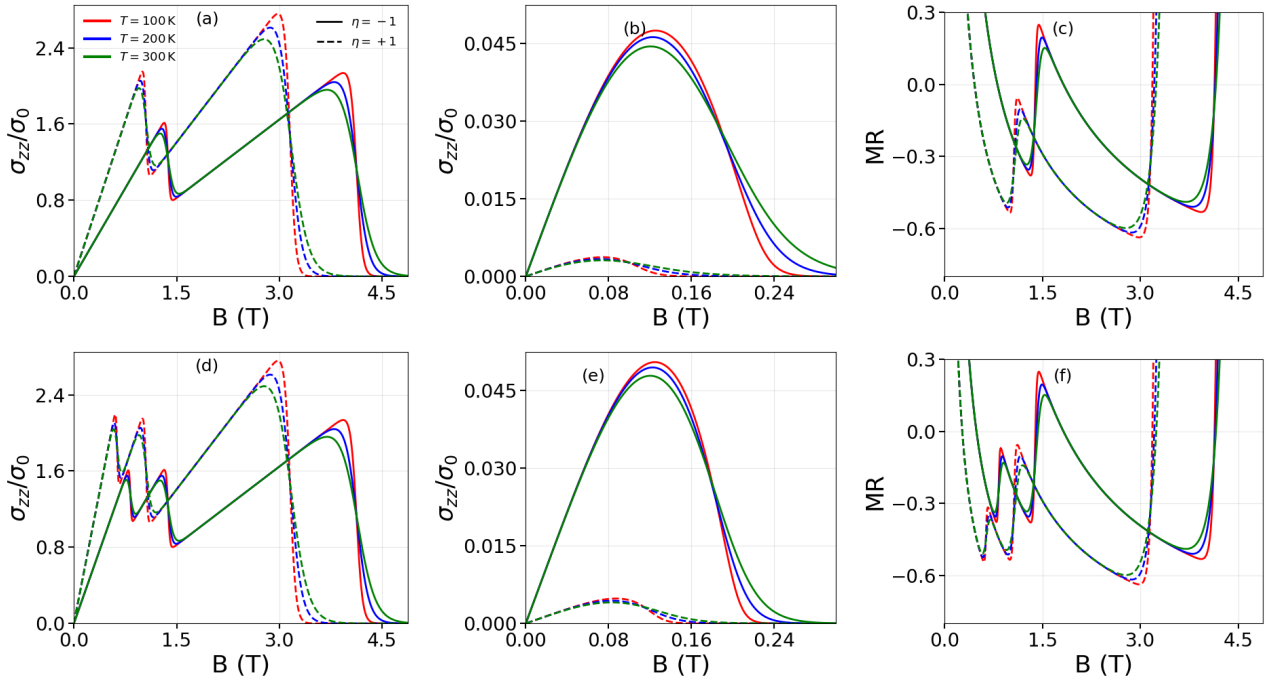


FIG. 2: (Color online) Magnetotransport response of multi-Weyl semimetals for the double-Weyl ($m = 2$) and triple-Weyl ($m = 3$) cases. Red, blue, and green curves correspond to $T = 100, 200$, and 300 K , respectively. For $m = 2$, two chiral channels give rise to a two-stage linear increase in $\sigma_{zz}(B)$, while the bulk contribution (b) is confined to low fields, resulting in negative magnetoresistance (MR). For $m = 3$, three chiral channels produce three linear regimes in $\sigma_{zz}(B)$, with the bulk contribution (e) again negligible beyond small fields and a strongly negative MR.

The triple-Weyl case ($m = 3$) further accentuates these trends. Each of the three chiral levels contributes a well-defined linear segment in Fig. 2(d), leading to a characteristic three-step profile in the total conductivity. The bulk background shown in Fig. 2(e) again decays rapidly, reinforcing that bulk modes play a negligible role in the anomaly-driven regime. As a result, the MR curve in Fig. 2(f) is strongly negative and displays pronounced kinks marking the field values at which individual chiral branches are lifted above the Fermi energy. Such multi-step signatures are a direct fingerprint of the node's monopole charge and cannot be captured within semi-classical Boltzmann theories^{1,4}.

A convenient way to quantify the multi-step structure of the longitudinal conductivity is to identify the magnetic-field values at which each chiral Landau level crosses the Fermi energy. For a chiral branch indexed by n ($0 \leq n \leq m-1$), the condition $E_n^{\text{ch}}(k_z = 0) = E_F$ yields the characteristic field scale

$$B_n = \frac{E_F + (v_z - \eta w_z) \mathcal{Q}/2}{(2n+1) w_{\parallel}}, \quad (22)$$

where the factor $(2n+1)$ reflects the equally spaced offsets of the m chiral levels. These B_n values correspond directly to the kink locations in $\sigma_{zz}(B)$: once B exceeds B_n , the n^{th} chiral channel is pushed above the

Fermi level and no longer contributes to transport. In double- and triple-Weyl systems, the resulting sequence $\{B_0, B_1, \dots, B_{m-1}\}$ produces the two- and three-stage linear increase of $\sigma_{zz}(B)$ observed in Figs. 2(a) & (d), and the associated features in the MR curves in Figs. 2(c) & (f). Thus, the piecewise linear structure of $\sigma_{zz}(B)$ provides a direct transport fingerprint of the node's topological charge through the number of anomaly-active chiral modes.

Overall, Fig. 2 demonstrates that negative magnetoresistance in multi-Weyl semimetals arises from the combined effects of Landau quantization, the fixed number of chiral branches, and their field-independent scattering times. The linear-in- B growth of $\sigma_{zz}(B)$, the piecewise structure reflecting the monopole charge, and the rapid suppression of bulk contributions together provide a clear and robust quantum mechanical origin for the anomaly-driven MR response in Weyl and multi-Weyl systems.

As a consistency check, Fig. 3 shows the magnetotransport response for the single-Weyl case ($m = 1$). The chiral channel in Fig. 3(a) produces a single linear rise of $\sigma_{zz}(B)$, while the bulk contribution in the inset of Fig. 3(a) appears only at very small fields and rapidly vanishes due to strong impurity scattering. Consequently, the total conductivity is dominated entirely by the chiral level, yielding the monotonic negative MR shown in Fig. 3(b). This contrasts with the multi-step

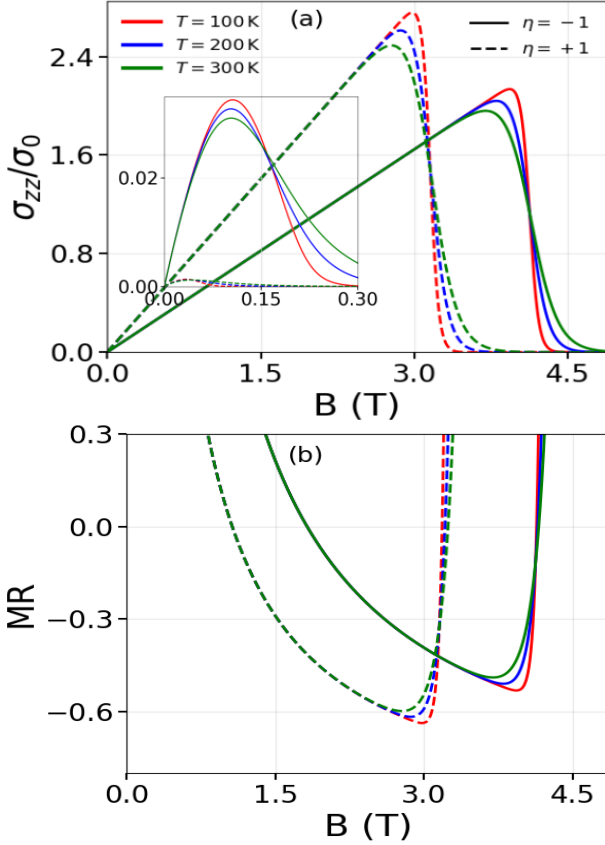


FIG. 3: (Color online) Magnetotransport response of a single-Weyl node ($m = 1$). Panel (a) shows the magnetic-field dependence of the normalized longitudinal conductivity σ_{zz}/σ_0 , dominated by the chiral channel. The inset highlights the contribution from non-chiral (bulk) ($n = m$) Landau level, which is confined to the low-field regime and remains negligibly small. Panel (b) shows the corresponding magnetoresistance (MR), which is negative over the entire field range shown.

structure observed for $m = 2$ and $m = 3$, confirming that the richer NMR profiles originate from the additional chiral channels of higher-charge nodes.

IV. CONCLUSION

We have developed a fully quantum-mechanical theory of negative magnetoresistance in Weyl and multi-Weyl semimetals based on their Landau-quantized spectrum and microscopic impurity scattering. Starting from the multi-Weyl Hamiltonian, we showed that the topological charge m determines the number of chiral Landau levels, each providing a unidirectional transport channel in the $\mathbf{E} \parallel \mathbf{B}$ configuration. Using screened Coulomb disorder within Fermi's golden rule and incorporating the resulting relaxation times into the Kubo formalism, we obtained closed-form expressions for the longitudinal con-

ductivity that capture the distinct roles of chiral and bulk Landau levels.

Our results demonstrate that the anomaly-driven magnetoconductivity is governed almost entirely by the chiral modes, whose field-independent scattering time and field-enhanced degeneracy produce a robust linear increase of $\sigma_{zz}(B)$. The number of linear segments directly reflects the monopole charge: single-, double-, and triple-Weyl nodes exhibit one, two, and three distinct slopes, respectively. Bulk Landau levels, by contrast, contribute only at very small fields due to their strong disorder sensitivity and rapidly decaying lifetimes. As a result, the magnetoresistance is strongly negative and displays characteristic kinks marking the depopulation of individual chiral branches.

This work provides a unified quantum description of chiral-anomaly-induced transport that goes beyond semi-classical formulations and makes clear predictions for experimental signatures in multi-Weyl systems. The multi-step NMR structure, the dominance of the chiral channels, and the rapid suppression of bulk contributions together offer a direct probe of the topological charge and Landau-level hierarchy in these materials. Our framework can be readily extended to include finite-tilt effects, interactions, and more realistic disorder profiles, opening the door to comprehensive quantum transport modeling of higher-order topological semimetals.

Acknowledgments: This work is an outcome of the Research work carried out under the SRG Project, SRG/2023/001516, Anusandhan National Research Foundation (ANRF), Government of India.

Appendix A: Impurity-limited self-energy

In this Appendix we derive the impurity-induced self-energy in the Landau-level basis $|n, k_z\rangle$ used throughout the main text. In the presence of a magnetic field, the impurity vertices and momentum routing are constrained by Landau quantization, which is encoded diagrammatically in Fig. 4. These diagrams determine the structure of the Dyson equation and directly fix the form of the quantum and transport scattering rates derived below.

We consider static screened Coulomb impurities located at random positions $\{\mathbf{R}_j\}$. The total impurity potential is $U(\mathbf{r}) = \sum_j \mathcal{V}(\mathbf{r} - \mathbf{R}_j)$, with Fourier transform $U(\mathbf{q}) = \mathcal{V}(\mathbf{q}) \sum_j e^{-i\mathbf{q} \cdot \mathbf{R}_j}$. For uncorrelated impurities of density n_i , disorder averaging yields

$$\langle U(\mathbf{q})U(\mathbf{q}') \rangle_{\text{dis}} = n_i |\mathcal{V}(\mathbf{q})|^2 (2\pi)^3 \delta(\mathbf{q} + \mathbf{q}'), \quad (\text{A1})$$

which enforces the momentum pairing $(\mathbf{q}, -\mathbf{q})$ along each impurity line in Fig. 4.

Screened Coulomb disorder: We model the impurity potential by a statically screened Coulomb interaction,

$$\mathcal{V}(\mathbf{q}) = \frac{4\pi e^2}{\varepsilon(q^2 + \kappa^2)}, \quad (\text{A2})$$

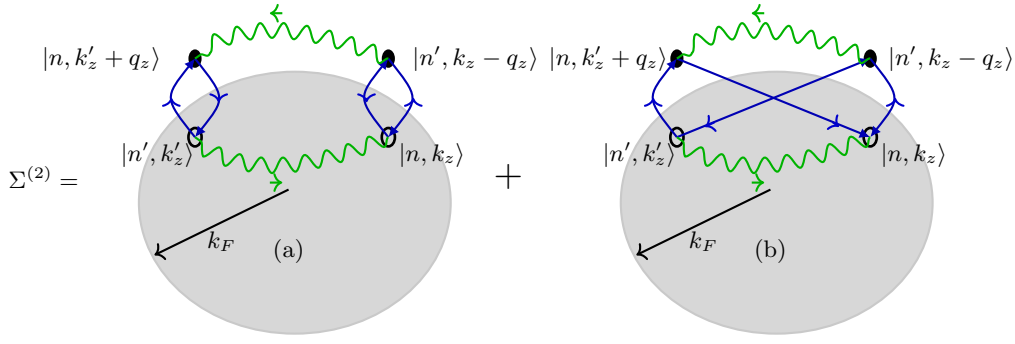


FIG. 4: Second-order impurity self-energy diagrams: (a) direct (Hartree) contribution, giving only a real energy shift; (b) exchange (crossed) contribution, producing the imaginary part of Σ^R and thus the impurity scattering rate.

where ε is the background dielectric constant and κ is the Thomas-Fermi screening wave vector. For a finite carrier density, κ follows from the static Lindhard expression,

$$\kappa^2 = \frac{4\pi e^2}{\varepsilon} \frac{\partial n_e}{\partial \mu} \Big|_{\mu=E_F} = \frac{4\pi e^2}{\varepsilon} \mathcal{D}(E_F). \quad (\text{A3})$$

For a representative Fermi energy $E_F = 200$ meV and magnetic fields relevant to this work, the Fermi level lies within the energy windows of the anomaly-active chiral Landau levels up to their depopulation fields. In this regime all m chiral branches contribute, reducing Eq. (12) to

$$\mathcal{D}_{\text{ch}}(E_F) \simeq \frac{m}{4\pi^2 l_B^2 |w_z - \eta v_z|}. \quad (\text{A4})$$

Substitution into Eq. (A3) yields

$$\kappa^2 = \frac{e^3 m B}{\pi \varepsilon \hbar |w_z - \eta v_z|}, \quad (\text{A5})$$

so that the Thomas-Fermi screening length scales as

$$\lambda_{\text{TF}} = \kappa^{-1} \propto (mB)^{-1/2}. \quad (\text{A6})$$

Using representative material parameters, we estimate $\lambda_{\text{TF}} \sim 1\text{-}3$ nm for $B \sim 1\text{-}4$ T, confirming that Coulomb disorder is efficiently screened in the anomaly-dominated regime.

Impurity vertex and Dyson equation: In a magnetic field the eigenstates factorize as $|n, k_z\rangle = |n\rangle_{\perp} \otimes |k_z\rangle$. The impurity vertex therefore takes the form

$$\langle n, k_z | e^{i\mathbf{q} \cdot \mathbf{r}} | n', k'_z \rangle = \delta_{k'_z, k_z - q_z} \mathcal{F}_{nn'}(\mathbf{q}_{\perp}), \quad (\text{A7})$$

which enforces longitudinal momentum transfer q_z and Landau-level mixing through the form factor $\mathcal{F}_{nn'}$. These constraints are represented graphically in Fig. 4.

The disorder-averaged Green's function satisfies the Dyson equation

$$G = G_0 + G_0 \Sigma G, \quad (\text{A8})$$

which generates the two second-order diagrams shown in Fig. 4. The direct (Hartree) diagram produces only a real, momentum-independent energy shift and does not contribute to level broadening or transport. It will therefore not be considered further.

The exchange diagram, Fig. 4(b), contains a genuine momentum exchange between the two fermionic trajectories. Evaluating the vertices using Eq. (A7), one obtains the retarded self-energy

$$\Sigma_n^R(k_z, \omega) = \frac{N_i}{V} \sum_{n'} \sum_{\mathbf{q}} |\mathcal{V}(\mathbf{q})|^2 |\mathcal{F}_{nn'}(\mathbf{q}_{\perp})|^2 C_{n'}^R(k_z - q_z, \omega), \quad (\text{A9})$$

which directly corresponds to diagram (b).

Quantum and transport lifetimes. The imaginary part of Eq. (A9), evaluated on shell, determines the quantum lifetime,

$$\frac{1}{\tau_n^{\text{q}}(k_z)} = 2\pi \frac{N_i}{V} \sum_{n'} \sum_{\mathbf{q}} |\mathcal{V}(\mathbf{q})|^2 |\mathcal{F}_{nn'}(\mathbf{q}_{\perp})|^2 \times \delta[\varepsilon_n(k_z) - \varepsilon_{n'}(k_z - q_z)]. \quad (\text{A10})$$

The transport lifetime is obtained by including the usual factor $(1 - \cos \theta)$, which suppresses forward scattering,

$$\frac{1}{\tau_n^{\text{tr}}(k_z)} = 2\pi \frac{N_i}{V} \sum_{n'} \sum_{\mathbf{q}} |\mathcal{V}(\mathbf{q})|^2 |\mathcal{F}_{nn'}(\mathbf{q}_{\perp})|^2 (1 - \cos \theta) \times \delta[\varepsilon_n(k_z) - \varepsilon_{n'}(k_z - q_z)]. \quad (\text{A11})$$

Only τ_n^{tr} enters the Kubo conductivity.

Validity of the Born approximation: The second-order Born expansion is controlled provided the disorder-induced broadening $\Gamma_n = -\text{Im } \Sigma_n^R$ remains small compared to the Landau-level spacing. For chiral levels this spacing is $\Delta_n = E_{n+1}^{\text{ch}} - E_n^{\text{ch}} = 2Bw_{\parallel}$, and we require $\Gamma_n \ll \Delta_n$. Using the screened potential (A2), we find that Γ_n decreases with field for chiral modes and grows only weakly for bulk levels due to the rapid decay of the form factors. For impurity densities $n_{\text{imp}} = 10^{16}\text{-}10^{18} \text{ cm}^{-3}$, this condition is satisfied for all fields $B \gtrsim 0.5$ T.

1. Derivation of the form factor $\mathcal{F}_{nn'}(\mathbf{q}_\perp)$:

For Chiral states : The Landau-level eigenstate for the chiral states takes the spinor of the form

$$|\psi_n^{\text{ch}}\rangle = \begin{pmatrix} 0 \\ |n\rangle \end{pmatrix} \otimes |k_x, k_z\rangle.$$

To obtain the position-space representation, we use the standard relations $\langle x|k_x\rangle = e^{ik_x x}/\sqrt{L_x}$, $\langle z|k_z\rangle = e^{ik_z z}/\sqrt{L_z}$, and $\langle y|n\rangle = c_n/\sqrt{l_B} e^{-\zeta^2/2} \mathcal{H}_n(\zeta)$, with $c_n = 1/\sqrt{2^n n! \sqrt{\pi}}$ and

$\mathcal{H}_n(\zeta)$ being the Hermite polynomial of degree n .

Putting these results together, the chiral state's real-space wavefunction, written in Schroedinger notation, takes the form

$$\psi_n^{\text{ch}}(\mathbf{r}) = \frac{c_n}{\sqrt{L_x L_z l_B}} e^{ik_x x} e^{ik_z z} e^{-\frac{(y-y_0)^2}{2l_B^2}} \mathcal{H}_n\left(\frac{y-y_0}{l_B}\right) \quad (\text{A12})$$

where we have defined $y_0 = k_x l_B^2$.

Using the explicit form of the wavefunctions, the matrix element becomes

$$\begin{aligned} \langle \psi_n^{\text{ch}} | U | \psi_{n'}^{\text{ch}} \rangle &= \sum_i \int \frac{d^3 r}{L_x L_z} \psi_{n'}^*(y) \mathcal{V}(\mathbf{r} - \mathbf{R}_i) \psi_n(y) e^{i(k_x - k'_x)x} e^{i(k_z - k'_z)z} \\ &= \sum_i (2\pi \delta_{q_x, k_x - k'_x})(2\pi \delta_{q_z, k_z - k'_z}) \int \frac{d^3 q}{(2\pi)^3} \mathcal{V}(\mathbf{q}) e^{-i\mathbf{q} \cdot \mathbf{R}_i} \int dy \psi_{n'}^*(y) \psi_n(y) e^{iq_y y}. \end{aligned} \quad (\text{A13})$$

We separate out the non-trivial y -integral,

$$I_y^c = \frac{c_n c_{n'}}{l_B} \int_{-\infty}^{\infty} e^{-(y-y_0)^2/2l_B^2} e^{-(y-y'_0)^2/2l_B^2} \mathcal{H}_n\left(\frac{y-y_0}{l_B}\right) \mathcal{H}_{n'}\left(\frac{y-y'_0}{l_B}\right) e^{iq_y y} dy. \quad (\text{A14})$$

Using the exact Hermite-polynomial identity

$$\int_{-\infty}^{\infty} e^{-x^2} \mathcal{H}_n(x+a) \mathcal{H}_m(x+b) dx = 2^n \sqrt{\pi} n! (b-a)^{|m-n|} \mathcal{L}_n^{|m-n|}(-2ab) \quad (\text{A15})$$

we find an analytical expression involving associated Laguerre polynomials. A more compact form uses $q_\perp = \frac{l_B^2}{2}(q_x^2 + q_y^2)$, leading to

$$I_y^c = \sqrt{\frac{n_{<}!}{n_{>}!}} e^{iq_y(y_0+y'_0)/2} e^{-q_\perp/2} \left[\frac{l_B}{2} (q_x + iq_y) \right]^{|n-n'|} \mathcal{L}_{n_{<}}^{|n-n'|}(q_\perp). \quad (\text{A16})$$

For chiral self-scattering (i.e., $n = n'$), this simplifies to $I_y = e^{iq_y(y_0+y'_0)/2} e^{-q_\perp/2} \mathcal{L}_n(q_\perp)$, thus giving us

$$\langle \psi_n^{\text{ch}} | U | \psi_{n'}^{\text{ch}} \rangle = \sum_i (2\pi)^2 \delta_{q_x, k_x - k'_x} \delta_{q_z, k_z - k'_z} \sqrt{\frac{n_{<}!}{n_{>}!}} e^{iq_y(y_0+y'_0)/2} e^{-q_\perp/2} \left[\frac{l_B}{2} (q_x + iq_y) \right]^{|n-n'|} \mathcal{L}_{n_{<}}^{|n-n'|}(q_\perp) \int \frac{d^3 q}{(2\pi)^3} \mathcal{V}(\mathbf{q}) e^{-i\mathbf{q} \cdot \mathbf{R}_i}$$

We can write

$$\mathcal{F}_{nn'}(\mathbf{q}_\perp) = \sqrt{\frac{n_{<}!}{n_{>}!}} e^{iq_y(y_0+y'_0)/2} e^{-q_\perp/2} \left[\frac{l_B}{2} (q_x + iq_y) \right]^{|n-n'|} \mathcal{L}_{n_{<}}^{|n-n'|}(q_\perp) \quad (\text{A17})$$

Using the above results in Eq. A11, we obtained the inverse relaxation time states $1/\tau^{\text{tr}}$ as

$$\frac{1}{\tau^{\text{tr}}} = \frac{n_{\text{imp}}}{2k_F^2} \frac{1}{|w_z - \eta v_z|} \int_0^\infty dq_\perp \frac{q_\perp e^{-q_\perp} [\mathcal{L}_n(q_\perp)]^2}{\left(q_\perp + \frac{1}{4\pi^2 |w_z - \eta v_z|} \right)^2}, \quad (\text{A18})$$

which can be expressed in terms of $\mathcal{I}_n^{\eta, \text{ch}}$ as

$$\tau^{\text{tr}} = \frac{\tau_0}{\mathcal{I}_n^{\eta, \text{ch}}}, \quad (\text{A19})$$

with $\tau_0 = \frac{2k_F^2 V \epsilon |w_z - \eta v_z|}{n_{\text{imp}}}$ and we have defined

$$\mathcal{I}_n^{\eta, \text{ch}} = \int_0^\infty dq_\perp \frac{q_\perp e^{-q_\perp} [\mathcal{L}_n(q_\perp)]^2}{\left(q_\perp + \frac{1}{4\pi^2 |w_z - \eta v_z|}\right)^2}. \quad (\text{A20})$$

For Bulk states: We can similarly write the real-space wavefunction (in Schrodinger notation) for a bulk state $n \geq m$ in conduction band as,

$$\psi_n^b(\mathbf{r}) = \frac{c_n}{\sqrt{L_x L_z l_B}} e^{ik_x x} e^{ik_z z} e^{-\frac{(y-y_0)^2}{2l_B^2}} [\alpha_n + \beta_n \mathcal{H}_n\left(\frac{y-y_0}{l_B}\right)]. \quad (\text{A21})$$

We drop the η, s indices from the wavefunction, noting that the above equation pertains to a bulk state in the conduction band of a particular chirality. Everything in $\langle \psi_n^b | U | \psi_{n'}^b \rangle$ will remain unchanged except the y-integral, thus yielding the form factor,

$$\mathcal{F}_{nn'}(\mathbf{q}_\perp) = \frac{c_n c_{n'}}{l_B} \int_{-\infty}^\infty e^{-(y-y_0)^2/2l_B^2} e^{-(y-y_0')^2/2l_B^2} [\alpha_n + \beta_n \mathcal{H}_n\left(\frac{y-y_0}{l_B}\right)][\alpha_{n'} + \beta_{n'} \mathcal{H}_{n'}\left(\frac{y-y_0'}{l_B}\right)] e^{iq_y y} dy \quad (\text{A22})$$

After solving Eq. A22 by only taking the intra-level scattering $n = n'$, we have,

$$\mathcal{F}_{nn}(\mathbf{q}_\perp) = e^{-q_\perp/2 + iq_y(y_0+y_0')/2} [\mathcal{L}_n(q_\perp) + f_n(q_\perp, \phi)]. \quad (\text{A23})$$

where for compactness we define, $f_n(q_\perp, \phi) = \begin{cases} \frac{2^{-n} \alpha_n (\alpha_n + 2l_B^n \beta_n q^n \cos \phi)}{n!}, & n \text{ even}, \\ \frac{2^{-n} \alpha_n (\alpha_n + 2l_B^n \beta_n q^n \sin \phi)}{n!}, & n \text{ odd}. \end{cases}$

Using the above results in Eq. A11, and using the replacement $\sum_{\mathbf{q}} \rightarrow \frac{V}{(2\pi)^3} \int dq_z \int_0^\infty \frac{2}{l_B^2} dq_\perp \int_0^{2\pi} d\phi$, we obtain the inverse relaxation time for the bulk state, $|m, k_z\rangle$, as,

$$\frac{1}{\tau_n^{\text{tr}}(k_z)} = \frac{2\pi n_i}{(2\pi)^3} \int dq_z \int_0^\infty \frac{2}{l_B^2} dq_\perp \int_0^{2\pi} d\phi |\mathcal{V}(\mathbf{q})|^2 \frac{\frac{2}{l_B^2} q_\perp + q_z^2}{k_f^2} e^{-q_\perp} [\mathcal{L}_n^2 + 2\mathcal{L}_n f_n + f_n^2] \delta(\varepsilon_n(k_z) - \varepsilon_n(k_z - q_z)). \quad (\text{A24})$$

Using the linear expansion $\varepsilon_n(k_z) - \varepsilon_n(k_z - q_z) \simeq \left. \frac{\partial \varepsilon_n}{\partial k_z} \right|_{k_z} q_z \simeq (v_z + \eta w_z) q_z$, we obtain $\delta((v_z + \eta w_z) q_z) = \frac{1}{|(v_z + \eta w_z)|} \delta(q_z)$. Thus yielding the final expression

$$\frac{1}{\tau_n^{\text{tr}}(k_z)} = \frac{2n_i}{\pi |(v_z + \eta w_z)| k_f^2 l_B^4} \int_0^\infty q_\perp e^{-q_\perp} dq_\perp \int_0^{2\pi} d\phi |\mathcal{V}(q_\perp)|^2 [\mathcal{L}_n^2 + 2\mathcal{L}_n f_n + f_n^2]. \quad (\text{A25})$$

^{*} amawrie@iiti.ac.in

¹ D. T. Son and B. Z. Spivak, *Chiral anomaly and classical negative magnetoresistance of Weyl metals*, *Phys. Rev. B* **88**, 104412 (2013).

² A. A. Burkov, *Negative longitudinal magnetoresistance in Dirac and Weyl metals*, *Phys. Rev. B* **91**, 245157 (2015).

³ C. Zhang *et al.*, *Observation of the Adler-Bell-Jackiw anomaly in a Weyl semimetal*, *Nat. Commun.* **7**, 10735 (2016).

⁴ H.-J. Kim *et al.*, *Dirac versus Weyl Fermions in Topological Insulators: Adler-Bell-Jackiw Anomaly in Transport*

Phenomena, *Phys. Rev. Lett.* **111**, 246603 (2013).

⁵ X. Huang *et al.*, *Observation of the chiral anomaly induced negative magnetoresistance in 3D Weyl semimetal TaAs*, *Phys. Rev. X* **5**, 031023 (2015).

⁶ B. Z. Spivak and A. V. Andreev, *Magnetotransport phenomena related to the chiral anomaly in Weyl semimetals*, *Phys. Rev. B* **93**, 085107 (2016).

⁷ X. Wan, A. M. Turner, A. Vishwanath, and S. Y. Savrasov, *Topological semimetal and Fermi-arc surface states in the electronic structure of pyrochlore iridates*, *Phys. Rev. B* **83**, 205101 (2011).

⁸ A. A. Burkov and L. Balents, *Weyl semimetal in a topological insulator multilayer*, *Phys. Rev. Lett.* **107**, 127205 (2011).

⁹ N. P. Armitage, E. J. Mele, and A. Vishwanath, *Weyl and Dirac semimetals in three-dimensional solids*, *Rev. Mod. Phys.* **90**, 015001 (2018).

¹⁰ B. Yan and C. Felser, *Topological materials: Weyl semimetals*, *Annu. Rev. Condens. Matter Phys.* **8**, 337 (2017).

¹¹ H. B. Nielsen and M. Ninomiya, *The Adler-Bell-Jackiw anomaly and Weyl fermions in a crystal*, *Phys. Lett. B* **130**, 389 (1983).

¹² A. A. Burkov, *Anomalous Hall Effect in Weyl metals*, *Phys. Rev. Lett.* **113**, 187202 (2014).

¹³ C. Fang, M. J. Gilbert, X. Dai, and B. A. Bernevig, "Multi-Weyl Topological Semimetals Stabilized by Point Group Symmetry," *Phys. Rev. Lett.* **108**, 266802 (2012).

¹⁴ C. Fang, M. J. Gilbert, and B. A. Bernevig, *Bulk topological invariants in noninteracting point group symmetric insulators*, *Phys. Rev. B* **86**, 115112 (2012).

¹⁵ Y. Sun and A. M. Wang, Y. Lai, H. H. Lai, and W. F. Tsai, *Magneto-optical conductivity of double Weyl semimetals*, *Phys. Rev. B* **96**, 085147 (2017).

¹⁶ H. Weng, C. Fang, Z. Fang, B. A. Bernevig, and X. Dai, *Weyl Semimetal Phase in Noncentrosymmetric Transition-Metal Monophosphides*, *Phys. Rev. X* **5**, 011029 (2015).

¹⁷ Y. Xu, Z. Song, Z. Wang, H. Weng, and X. Dai, *Higher-Order Topology of the Axion Insulator EuIn₂As₂*, *Phys. Rev. Lett.* **122**, 255402 (2019).

¹⁸ S. Kimura, Y. Nakajima, Z. Mita, R. Jha, R. Higashinaka, T. D. Matsuda, Y. Aoki, *Optical evidence of type-II Weyl semimetals MoTe₂ and WTe₂*, *Phys. Rev. B* **99**, 195203 (2019).

¹⁹ Su-Yang Xu *et al.*, *Discovery of Lorentz-violating type II Weyl fermions in LaAlGe*, *Science Advances* **3**, e1603266 (2017).

²⁰ G. Chang *et al.*, *Unconventional Chiral Fermions and Large Topological Fermi Arcs in RhSi*, *Phys. Rev. Lett.* **119**, 206401 (2017).

²¹ E. Liu *et al.*, *Giant anomalous Hall effect in a ferromagnetic kagome-lattice semimetal*, *Nature Physics* **14**, 1125-1131 (2018).

²² J. Y. Liu *et al.*, *A magnetic topological semimetal Sr_{1-y}Mn_{1-z}Sb₂ (y,z<0.1)*, *Nature Materials*, **16**, 905-910 (2017).

²³ G. Chang *et al.*, *Topological quantum properties of chiral crystals*, *Nature Materials* **17**, 978- 985 (2018).

²⁴ N. B. M. Schröter *et al.*, *Chiral topological semimetal with multifold band crossings and long Fermi arcs*, *Nature Physics* **15**, 759-765 (2019).

²⁵ B. Q. Lv *et al.*, "Observation of Weyl nodes in TaAs," *Nat. Phys.* **11**, 724 (2015).

²⁶ S. Y. Xu *et al.*, "Discovery of a Weyl fermion state with Fermi arcs in niobium arsenide," *Nat. Phys.* **11**, 748-754 (2015).

²⁷ L. X. Yang *et al.*, "Weyl semimetal phase in the noncentrosymmetric compound TaAs," *Nat. Phys.* **11**, 728 (2015).

²⁸ S.-M. Huang *et al.*, "New type of Weyl semimetal with quadratic doubleWeyl fermions," *Proc. Natl. Acad. Sci. USA* **113**, 1180 (2015).

²⁹ P. Tang, Q. Zhou, and S.-C. Zhang, "Multiple types of topological fermions in transition metal silicides," *Phys. Rev. Lett.* **119**, 206402 (2017).

³⁰ N. B. M. Schröter *et al.*, "Topological chiral crystals with multifold band crossings and long Fermi arcs," *Nat. Phys.* **15**, 759-765 (2019).

³¹ S. Tchoumakov, M. Civelli, and M. O. Goerbig, "Magnetic-field-driven relativistic properties in type-I and type-II Weyl semimetals," *Phys. Rev. Lett.* **117**, 086402 (2016).

³² A. A. Soluyanov, D. Gresch, Z. Wang, Q. Wu, M. Troyer, X. Dai, and B. A. Bernevig, "Type-II Weyl semimetals," *Nature* **527**, 495-498 (2015).

³³ Sushmita Saha, Deepannita Das, Alestin Mawrie, *Unveiling the Chiral States in Multi-Weyl Semimetals through Magneto-Optical Spectroscopy*, *J. Phys.: Condens. Matter* **37**, 405702 (2025).

³⁴ X. Yuan, *et al.*, "Chiral Landau levels in Weyl semimetal NbAs with multiple topological carriers," *Nat. Commun.* **9**, 1854 (2018).

³⁵ P.-L. Zhao, X.-B. Qiang, H.-Z. Lu, and X. C. Xie, "Coulomb Instabilities of a Three-Dimensional Higher-Order Topological Insulator", *Phys. Rev. Lett.* **127**, 176601 (2021).

³⁶ H. Bruus and K. Flensberg, *Many-Body Quantum Theory in Condensed Matter Physics: An Introduction*, Oxford Graduate Texts, Oxford University Press, Oxford, 2004. ISBN: 978-0-19-856633-5.

³⁷ J. Rammer, *Quantum Field Theory of Non-equilibrium States* (Cambridge University Press, 2007).

³⁸ D. A. Greenwood, "The Boltzmann equation in the theory of electrical conduction in metals," *Proc. Phys. Soc.* **71**, 585 (1958).

³⁹ A. A. Burkov and L. Balents, "Weyl semimetal in a topological insulator multilayer," *Phys. Rev. Lett.* **107**, 127205 (2011).

⁴⁰ I. Crassee *et al.*, "BiTeCl and BiTeBr: A comparative high-pressure optical study", *Phys. Rev. B* **95**, 045201 (2017).

⁴¹ G. Sharma, P. Goswami, and S. Tewari, "Chiral anomaly and longitudinal magnetotransport in type-II Weyl semimetals", *Phys. Rev. B* **96**, 045112 (2017).